Anatomical assessment of trigeminal nerve tractography using diffusion MRI: A comparison of acquisition b-values and single- and multi-fiber tracking strategies

Xie, Guoqiang ; Zhang, Fan ; Leung, Laura ; Mooney, Michael A ; Epprecht, Lorenz ; Norton, Isaiah ; Rathi, Yogesh ; Kikinis, Ron ; Al-Mefty, Ossama ; Makris, Nikos ; Golby, Alexandra J ; O'Donnell, Lauren J

Abstract: Background: The trigeminal nerve (TGN) is the largest cranial nerve and can be involved in multiple inflammatory, compressive, ischemic or other pathologies. Currently, imaging-based approaches to identify the TGN mostly rely on T2-weighted magnetic resonance imaging (MRI), which provides localization of the cisternal portion of the TGN where the contrast between nerve and cerebrospinal fluid (CSF) is high enough to allow differentiation. The course of the TGN within the brainstem as well as anterior to the cisternal portion, however, is more difficult to display on traditional imaging sequences. An advanced imaging technique, diffusion MRI (dMRI), enables tracking of the trajectory of TGN fibers and has the potential to visualize anatomical regions of the TGN not seen on T2-weighted imaging. This may allow a more comprehensive assessment of the nerve in the context of pathology. To date, most work in TGN tracking has used clinical dMRI acquisitions with a b-value of 1000 s/mm2 and conventional diffusion tensor MRI (DTI) tractography methods. Though higher b-value acquisitions and multi-tensor tractography methods are known to be beneficial for tracking brain white matter fiber tracts, there have been no studies conducted to evaluate the performance of these advanced approaches on nerve tracking of the TGN, in particular on tracking different anatomical regions of the TGN. Objective: We compare TGN tracking performance using dMRI data with different b-values, in combination with both single- and multi-tensor tractography methods. Our goal is to assess the advantages and limitations of these different strategies for identifying the anatomical regions of the TGN. Methods: We proposed seven anatomical rating criteria including true and false positive structures, and we performed an expert rating study of over 1000 TGN visualizations, as follows. We tracked the TGN using high-quality dMRI data from 100 healthy adult subjects from the Human Connectome Project (HCP). TGN tracking performance was compared across dMRI acquisitions with b = 1000 s/mm2, b = 2000 s/mm2 and b = 3000 s/mm2, using single-tensor (1T) and two-tensor (2T) unscented Kalman filter (UKF) tractography. This resulted in a total of six tracking strategies. The TGN was identified using an anatomical region-of-interest (ROI) selection approach. First, in a subset of the dataset we identified ROIs that provided good TGN tracking performance across all tracking strategies. Using these ROIs, the TGN was then tracked in all subjects using the six tracking strategies. An expert rater (GX) visually assessed and scored each TGN based on seven anatomical judgment criteria. These criteria included the presence of multiple expected anatomical segments of the TGN (true positive structures), specifically branch-like structures, cisternal portion, mesencephalic trigeminal tract, and spinal cord tract of the TGN. False positive criteria included the presence of any fibers entering the temporal lobe, the inferior cerebellar peduncle, or the middle cerebellar peduncle. Expert rating scores were analyzed to compare TGN tracking performance across the six tracking strategies. Intra- and inter-rater validation was performed to assess the reliability of the expert TGN rating result.

DOI: https://doi.org/10.1016/j.nicl.2019.102160

Originally published at:
Xie, Guoqiang; Zhang, Fan; Leung, Laura; Mooney, Michael A; Epprecht, Lorenz; Norton, Isaiah; Rathi, Yogesh; Kikinis, Ron; Al-Mefty, Ossama; Makris, Nikos; Golby, Alexandra J; O'Donnell, Lauren J (2020). Anatomical assessment of trigeminal nerve tractography using diffusion MRI: A comparison of acquisition b-values and single- and multi-fiber tracking strategies. NeuroImage: Clinical, 25:102160.
DOI: https://doi.org/10.1016/j.nicl.2019.102160

NeuroImage: Clinical 25 (2020) 102160

Contents lists available at ScienceDirect

NeuroImage: Clinical

journal homepage: www.elsevier.com/locate/ynicl

Anatomical assessment of trigeminal nerve tractography using diffusion MRI: A comparison of acquisition *b*-values and single- and multi-fiber tracking strategies

Guoqiang Xie[a,b,1], Fan Zhang[b,1,*], Laura Leung[b,c,d], Michael A. Mooney[c], Lorenz Epprecht[e], Isaiah Norton[b], Yogesh Rathi[b,f], Ron Kikinis[b], Ossama Al-Mefty[c], Nikos Makris[f,g], Alexandra J. Golby[b,c], Lauren J O'Donnell[b]

[a] Department of Neurosurgery, Nuclear Industry 215 Hospital of Shaanxi Province, Xianyang, China
[b] Department of Radiology, Brigham and Women's Hospital, Harvard Medical School, Boston, USA
[c] Department of Neurosurgery, Brigham and Women's Hospital, Harvard Medical School, Boston, USA
[d] Faculty of Medicine, The Chinese University of Hong Kong, Hong Kong, China
[e] Department of Otolaryngology, Head and Neck Surgery, University Hospital Zurich, Zurich, Switzerland
[f] Department of Psychiatry, Brigham and Women's Hospital, Harvard Medical School, Boston, USA
[g] Departments of Psychiatry, Neurology and Radiology, Massachusetts General Hospital, Harvard Medical School, Boston, USA

ARTICLE INFO

Keywords:
Trigeminal nerve
Trigeminal neuralgia
Diffusion MRI
Diffusion tensor imaging
Single-tensor tractography
Multi-tensor tractography

ABSTRACT

Background: The trigeminal nerve (TGN) is the largest cranial nerve and can be involved in multiple inflammatory, compressive, ischemic or other pathologies. Currently, imaging-based approaches to identify the TGN mostly rely on T2-weighted magnetic resonance imaging (MRI), which provides localization of the cisternal portion of the TGN where the contrast between nerve and cerebrospinal fluid (CSF) is high enough to allow differentiation. The course of the TGN within the brainstem as well as anterior to the cisternal portion, however, is more difficult to display on traditional imaging sequences. An advanced imaging technique, diffusion MRI (dMRI), enables tracking of the trajectory of TGN fibers and has the potential to visualize anatomical regions of the TGN not seen on T2-weighted imaging. This may allow a more comprehensive assessment of the nerve in the context of pathology. To date, most work in TGN tracking has used clinical dMRI acquisitions with a *b*-value of 1000 s/mm^2 and conventional diffusion tensor MRI (DTI) tractography methods. Though higher *b*-value acquisitions and multi-tensor tractography methods are known to be beneficial for tracking brain white matter fiber tracts, there have been no studies conducted to evaluate the performance of these advanced approaches on nerve tracking of the TGN, in particular on tracking different anatomical regions of the TGN.

Objective: We compare TGN tracking performance using dMRI data with different *b*-values, in combination with both single- and multi-tensor tractography methods. Our goal is to assess the advantages and limitations of these different strategies for identifying the anatomical regions of the TGN.

Methods: We proposed seven anatomical rating criteria including true and false positive structures, and we performed an expert rating study of over 1000 TGN visualizations, as follows. We tracked the TGN using high-quality dMRI data from 100 healthy adult subjects from the Human Connectome Project (HCP). TGN tracking performance was compared across dMRI acquisitions with $b = 1000$ s/mm^2, $b = 2000$ s/mm^2 and $b = 3000$ s/mm^2, using single-tensor (1T) and two-tensor (2T) unscented Kalman filter (UKF) tractography. This resulted in a total of six tracking strategies. The TGN was identified using an anatomical region-of-interest (ROI) selection approach. First, in a subset of the dataset we identified ROIs that provided good TGN tracking performance across all tracking strategies. Using these ROIs, the TGN was then tracked in all subjects using the six tracking strategies. An expert rater (GX) visually assessed and scored each TGN based on seven anatomical judgment criteria. These criteria included the presence of multiple expected anatomical segments of the TGN (true positive structures), specifically branch-like structures, cisternal portion, mesencephalic trigeminal tract, and spinal cord tract of the TGN. False positive criteria included the presence of any fibers entering the temporal lobe, the inferior cerebellar peduncle, or the middle cerebellar peduncle. Expert rating scores were analyzed to compare

* Corresponding author.
E-mail address: fzhang@bwh.harvard.edu (F. Zhang).
[1] G. Xie and F. Zhang contributed equally to the study, and are co-first authors of this paper.

https://doi.org/10.1016/j.nicl.2019.102160
Received 19 September 2019; Received in revised form 26 December 2019; Accepted 28 December 2019
Available online 08 January 2020

TGN tracking performance across the six tracking strategies. Intra- and inter-rater validation was performed to assess the reliability of the expert TGN rating result.

Results: The TGN was selected using two anatomical ROIs (Meckel's Cave and cisternal portion of the TGN). The two-tensor tractography method had significantly better performance on identifying true positive structures, while generating more false positive streamlines in comparison to the single-tensor tractography method. TGN tracking performance was significantly different across the three *b*-values for almost all structures studied. Tracking performance was reported in terms of the percentage of subjects achieving each anatomical rating criterion. Tracking of the cisternal portion and branching structure of the TGN was generally successful, with the highest performance of over 98% using two-tensor tractography and $b = 1000$ or $b = 2000$. However, tracking the smaller mesencephalic and spinal cord tracts of the TGN was quite challenging (highest performance of 37.5% and 57.07%, using two-tensor tractography with $b = 1000$ and $b = 2000$, respectively). False positive connections to the temporal lobe (over 38% of subjects for all strategies) and cerebellar peduncles (100% of subjects for all strategies) were prevalent. High joint probability of agreement was obtained in the inter-rater (on average 83%) and intra-rater validation (on average 90%), showing a highly reliable expert rating result.

Conclusions: Overall, the results of the study suggest that researchers and clinicians may benefit from tailoring their acquisition and tracking methodology to the specific anatomical portion of the TGN that is of the greatest interest. For example, tracking of branching structures and TGN-T2 overlap can be best achieved with a two-tensor model and an acquisition using $b = 1000$ or $b = 2000$. In general, $b = 1000$ and $b = 2000$ acquisitions provided the best-rated tracking results. Further research is needed to improve both sensitivity and specificity of the depiction of the TGN anatomy using dMRI.

dMRI:	diffusion magnetic resonance imaging
DWI:	diffusion weighted imaging
DTI:	diffusion tensor imaging
TGN:	trigeminal nerve
TN:	trigeminal neuralgia
ROI:	region of interest
MC:	Meckel's Cave
CP:	cisternal portion of trigeminal nerve
REZ:	root entry zone
ICP:	inferior cerebellar peduncle
MCP:	middle cerebellar peduncle

1. Introduction

The trigeminal nerve (TGN) is the largest cranial nerve in the brain. It includes five segments (brainstem, cisternal, Meckel's cave (MC), cavernous sinus and peripheral divisions) and contains both sensory and motor components (Go et al., 2001; Joo et al., 2014). Because of the extensive nerve distribution territory, multiple diseases can affect the TGN at different regions along the course of the TGN (Bathla and Hegde, 2013; Woolfall and Coulthard, 2001). Even for trigeminal neuralgia (TN), the most common disorder of the TGN, the pathogenesis is as diverse as neurovascular compression (Love and Coakham, 2001; Suzuki et al., 2015; Yadav et al., 2017), multiple sclerosis (Love and Coakham, 2001; Yadav et al., 2017), space-occupying lesions (Cruccu et al., 2016; Maarbjerg et al., 2017), local ischemia (Balestrino and Leandri, 1997; Golby et al., 1998), viral infection (Rousseau et al., 2015) and traumatic brain injury (Haviv et al., 2014). A detailed understanding of the TGN anatomy is essential for an accurate diagnosis and optimal choice of treatment options for TN.

Multiple magnetic resonance imaging (MRI) techniques have been used to identify the TGN for clinical and research purposes. Among these techniques, traditional T2-weighted MRI is the most widely used, e.g., to confirm the presence of neurovascular compression at the root entry zone (REZ) of the TGN (Casselman et al., 2008). There have also been studies applying MRI techniques, such as constructive interference in steady-state sequence, fast imaging employing steady-state acquisition and driven equilibrium radio frequency reset pulse, which have advanced performance in visualizing human nerves compared to a conventional T2-weighted image (Ciftci et al., 2004; Ruiz-Juretschke et al., 2018; Tsutsumi et al., 2018; Yoshino et al., 2003). However, these MRI sequences can only localize the cisternal portion of the TGN, while the continuity and pathological alteration of the TGN and brainstem nuclei, as well as the 3D relationship of the TGN with surrounding structures, cannot be assessed (Li et al., 2017; Liu et al., 2013; Neetu et al., 2016). Diffusion MRI (dMRI), via a process called tractography, can track brain white matter fibers in vivo non-invasively based on the principle of detecting the random motion of water molecules in neural tissue (Basser et al., 2000, 1994). dMRI tractography has been applied successfully for tracking of the cranial nerves (Fujiwara et al., 2011; Hung et al., 2017; Ishida et al., 2011; Jacquesson et al., 2018; Wei et al., 2016; Yoshino et al., 2016). One advantage of dMRI is that it enables tracking of the 3D trajectory of the TGN for a visualization of TGN structures not visualized by the aforementioned MRI sequences, e.g. the course of the TGN within the brainstem as well as anterior to the cisternal portion (Jacquesson et al., 2018). Multiple studies have investigated reconstruction of the TGN using dMRI tractography (Table 1).

Despite the success of dMRI for identification of the TGN, practical questions remain about what combination of acquisition, tractography method, and anatomical region of interest (ROI) selection will perform the best for identifying the TGN. In fact, a recent review came to the overall conclusion that research into different avenues of using dMRI is needed to optimize and improve the reliability of cranial nerve tractography, including the TGN (Shapey et al., 2019). To date, most work in TGN tractography has focused on clinical dMRI acquisitions using a *b*-value of 1000. Though higher *b*-values are known to be beneficial for tracking brain white matter fiber tracts (Descoteaux et al., 2007; Ning et al., 2015; Zhang et al., 2018), the performance of tractography resulting from different b-value acquisitions has not yet been studied for the TGN. In addition, the majority of TGN studies have used the diffusion tensor imaging (DTI) single-tensor model. Though higher-order models are known to be beneficial for more sensitive depiction of white matter fiber tracts in the brain (Baumgartner et al., 2012; Chen et al., 2016), work comparing the performance of fiber models in the TGN is limited thus far (Behan et al., 2017; Chen et al., 2016). Finally, ROI placement is variable across studies. In related work to perform selection of the TGN, most studies have adopted ROIs including cisternal portion (CP, also called prepontine cistern, cisternal segment or midpoint of the cisternal segment), and root entry zone (REZ) (Behan et al., 2017; Chen et al., 2011, 2016; Coskun et al., 2017; Fujiwara et al., 2011, 2007; Zolal et al., 2017). Fewer authors tracked the TGN using two ROIs including MC, REZ and the region adjacent to the brainstem (Hodaie et al., 2012; Moon et al., 2018; Wei et al., 2016; Zolal et al., 2017). Table 1 gives a summary of the ROI placement in these studies. Many studies have employed a single-ROI strategy; however, this strategy is unlikely to sufficiently restrict the fiber selection for more sensitive multi-fiber tractography methods (O'Donnell et al., 2017).

Table 1
Summary of existing TGN tracking studies using dMRI tractography.

Study	ROI placement	dMRI acquisition parameters	Fiber model
Kabasawa et al. (2007)	CP ("prepontine cistern")	TR/TE = 12000–15,000/70 ms; voxel size = NR (slice thickness 3 mm); number of directions = 6; *b*-value = 0/800 mm/s^2	DTI single-tensor
Fujiwara et al. (2011)	CP ("midpoint of the cisternal segment")	TR/TE = 8600/63 ms; voxel size = 1.6 × 1.6 × 1.2 mm; number of directions = 6; *b*-value = 0/1000 mm/s^2	DTI single-tensor
Chen et al. (2011)	REZ	TR/TE = 12,000/86.6 ms; voxel size = NR (slice thickness 3 mm); number of directions = 25; *b*-value = 0/1000 mm/s^2	DTI single-tensor
Hodaie et al. (2012)	Not reported	TR/TE = 12000/86.6 ms; voxel size = NR (slice thickness 3 mm); number of directions = 25; *b*-value = 0/1000 mm/s^2	DTI single-tensor
Yoshino et al. (2016)	CP	TR / TE = 9.916/157 ms; voxel size = 2.4 × 2.4 × 2.4 mm; number of directions = 101; *b*-values from 384 to 5000 mm/s^2 (DSI acquisition)	Orientation distribution function (ODF) using diffusion spectrum imaging
Chen et al. (2016)	REZ	TR/TE = 17,000/86.6 ms; voxel size = NR (slice thickness 3 mm); number of directions = 60; *b*-value = 0/1000 mm/s^2	DTI single-tensor; two-tensor
Wei et al. (2016)	MC + Tumor- brainstem surface	Not reported	Not reported
Behan et al. (2017)	CP ("retrogasserian portions of the nerve")	TR/TE = 88.6/17,000 ms; voxel size = NR (slice thickness 3 mm); number of directions = 60; *b*-value = 0/1000 mm/s^2	DTI single-tensor; two-tensor; constrained spherical deconvolution (CSD)
Coskun et al. (2017)	CP ("cisternal segments")	TR/TE = 3600/95 ms; voxel size = NR (slice thickness 4 mm); number of directions = 30; *b*-value = 0/1000	DTI single-tensor
Zolal et al. (2017)	MC ("ganglion") + Brainstem	(Healthy) TR/TE = 6281/67 ms; voxel size = NR; number of directions = 32; *b*-value = 0/700 mm/s^2 (Brain tumor patient) TR/TE = NR; voxel size = NR; number of directions = 20; *b*-value = 0/800 mm/s^2	DTI single-tensor
Hung et al. (2017)	Manually reconstructed without using ROIs	TR/TE = 17,000/86.4 ms; voxel size = 0.94 × 0.94 × 3 mm; number of directions = 60; *b*-value = 0/1000 mm/s^2	Two-tensor
Moon et al. (2018)	REZ + trigeminal nucleus	TR/ TE = 5606/63 ms; voxel size = 1.5 × 1.5 × 1.8 mm; number of directions = NR; *b*-value = 0/700 mm/s^2	DTI single-tensor

Abbreviations: CP-cisternal portion of trigeminal nerve, MC-Meckel's cave, REZ-root entry zone, NR-not reported.

The main contribution of this work is to investigate, for the first time, the performance of multiple acquisitions and fiber models for TGN identification. We leverage high-quality diffusion MRI data with several *b*-values from the Human Connectome Project (HCP) (Van Essen et al., 2013), and we experiment with two different fiber models available through the unscented Kalman filter (UKF) tractography package (Malcolm et al., 2010; Reddy and Rathi, 2016), which has been shown to provide high performance across multiple styles of dMRI acquisition (Zhang et al., 2018). Furthermore, we provide some insight into the choice of ROI for selecting the TGN, and we propose an expert rating system for quantitative assessment of the TGN, including both true positive and false positive criteria based on the known anatomy of the TGN. Intra- and inter-rater validation was performed to assess the reliability of the expert TGN rating result. While this initial exploration of strategies for TGN tractography is performed in healthy subjects, we expect that the results can be beneficial for improving TGN identification in clinical practice.

2. Materials and methods

2.1. Evaluation dataset

We used diffusion MR data from the HCP database (https://www.humanconnectome.org) (Van Essen et al., 2013) for experimental evaluation. The HCP database provides diffusion MR data that was acquired with a high quality image acquisition protocol using a customized Connectome Siemens Skyra scanner and processed using a well-designed processing pipeline (Glasser et al., 2013) including motion correction, eddy current correction and EPI distortion correction. We chose this high-quality and well-processed data to reduce any potential effects from data acquisition and data processing.

The acquisition parameters of the diffusion MR data in HCP were: TE = 89.5 ms, TR = 5520 ms, and voxel size = 1.25 × 1.25 × 1.25 mm^3. A total of 288 images were acquired in each dMRI dataset, including 18 baseline images with a low diffusion weighting b = 5 s/mm^2 and 270 diffusion weighted (DW) images evenly distributed at three shells of b = 1000/2000/3000 s/mm^2. In addition to the diffusion MR data, we also used the T2-weighted data (co-registered with the diffusion MR data), on which the TGN anatomical pathway was more visually apparent than on diffusion MR, for facilitating ROI selection on dMRI data (see Section 2.3 for details) and TGN tracking performance evaluation (see Section 2.5 for details). The acquisition parameters used for the T2-weighted data were TE = 565 ms, TR = 3200 ms, and voxel size = 0.7 × 0.7 × 0.7 mm^3. More detailed information about the HCP data acquisition and preprocessing can be found in (Glasser et al., 2013).

To enable assessment of performance of TGN tracking using acquisitions with different *b*-values, the multi-shell diffusion data of each subject was separated into single-shell b = 1000, b = 2000 and b = 3000 datasets. (We focused on acquisitions with a single b-value, consistent with the majority of current clinical dMRI acquisitions.) Each of these single-shell datasets consisted of 90 DW images and 18 baseline images. To assist in choosing tractography parameters (see Section 2.3 for details) and drawing ROIs (see Section 2.4 for details), diffusion tensor imaging (DTI) was computed for each single-shell dataset, as well as a trace map and a fractional anisotropy (FA) map derived from the computed DTI data. These computations were performed using the 3D Slicer software via the SlicerDMRI project (Norton et al., 2017).

In our study, we used the HCP 100 Unrelated Subjects data release that includes MR datasets from 100 healthy adult subjects. After a manual quality check of the diffusion data, we excluded 8 subjects from our analysis because their dMRI data had artifacts and/or noise at the skull base region that prevented placement of ROIs. (One subject had apparent signal drops ("black lines") at the skull base region. Seven subjects had image noise at the skull base region, in which we could not draw ROI in CP in four subjects and we could not draw ROI in MC in three subjects.) Therefore, datasets from 92 subjects (male/female: 41/51 individuals; age: 28.98 ± 2.81/28.96 ± 3.02 years) were included in our study, resulting in a total of 184 TGN tracts under study (bilateral TGN evaluation per subject).

2.2. TGN tracking using UKF tractography

We used the unscented Kalman filter (UKF) package (https://github.com/pnlbwh/ukftractography) (Malcolm et al., 2010; Reddy and Rathi, 2016) to perform TGN tracking. We chose the UKF tractography method because of its good performance in brain white matter fiber tracking (Chen et al., 2016; Gong et al., 2018; Liao et al., 2017; Zhang et al., 2018). In contrast to other methods that fit a model to the signal independently at each voxel (Behan et al., 2017; Qazi et al., 2009), in the UKF framework each tracking step employs prior information from the previous step to help stabilize model fitting. The UKF package provides both single-tensor (1T) and two-tensor (2T) fiber tracking methods, which enables a comparison between a single-tensor model and a higher-order model using the same underlying about 1 million fibers per dMRI scan using the same mathematical framework.

2.2.1. Experiment to determine best-performing tractography parameters

To compare across tracking strategies, we first performed an experiment to determine the best-performing tractography parameters for each combination of *b*-value and tensor model. The goal of this experiment was to provide an unbiased comparison across the different tracking strategies, because the best-performing tractography parameters can vary given the different SNR levels at different *b*-values and the single-tensor and two-tensor models.This was mainly due to the different SNR levels at different *b* values (Han et al. 2015), which required parameter adjustment specifically for each tracking strategy. (Our initial experimental results showed that using the same parameters could not provide a fair comparison across the different TGN tracking strategies, in terms of the percentage of the detected putative TGNs and tract visualization, as reported in Supplementary 1.) We tested a range of values (large enough to cover possible settings) to select the best-performing setting for the major parameters of the UKF method (see Supplementary Material 1 for details). All other parameters were set to the default values as suggested by the UKF software package. In this experiment, data from five randomly selected subjects were used for this parameter tuning. Expert raters (FZ and GX) visually assessed the obtained putative TGNs to select the settings that produced the best TGN according to the anatomical criteria introduced in Table 2.

2.2.2. Seeding TGN tractography in all datasets

Next, for each HCP subject, given the determined best-performance parameters (see Supplementary Table S1), 1T and 2T UKF tractography were seeded in each of the three single-shell dMRI datasets. A mask, which was larger than the possible region through which the TGN passes, was manually created by an expert (GX) using the 3D Slicer Segment Editor tool by placing a spherical or oval ROI with a radius of about 35 mm, centering at the anterior portion of the pons. This mask was larger than the possible region through which the TGN passes. Tractography was seeded from all voxels in this mask (two seeds per voxel). This procedure was similar to whole brain seeding but it was restricted to the potential TGN region for efficiency. This resulted in a total of six different tractography datasets per subject (1T-1000, 1T-1000, 1T-3000, 2T-1000, 2T-2000, and 2T-3000), which were further processed using defined ROIs for selection of the TGN (see Section 2.3 for details).

2.3. Selection of the TGN using ROIs

2.3.1. Experiment to determine best-performing ROIs

First, we conducted an experiment to determine a reasonable ROI or combination of ROIs for TGN selection across all tractography datasets. Three ROIs, including MC, CP and REZ, were compared. We note that these three ROIs were most commonly used in the literature (see Table 1), and they were relatively easy to be identified, in particular on the high-quality HCP data under study. In addition, the obtained ROIs were double checked on different images including the directionally encoded color (DEC) and trace maps of the $b = 1000$, $b = 2000$ and $b = 3000$ data, and the T2w image (see the next paragraph). Thus, we believe that potential effects from the manual ROI selection on the TGN tracking assessment were minimal. All possible selection approaches using these ROIs were tested, including single-ROI selection using only an individual ROI (*MC-only, CP-only, REZ-only*) and multi-ROI selection using combinations of different ROIs (*MC + CP, MC + REZ, CP + REZ* and *MC + CP + REZ*). In the multi-ROI selection methods, a streamline was selected to be a potential TGN steamlime only if it traversed all involved ROIs. Data from two randomly selected subjects was used in this experiment. For each of the compared TGN tracking strategies, 7 putative TGNs were obtained given the above 7 ROI-selection approaches. This resulted in a total of 84 putative TGNs (7 selections x 6 tracking strategies x 2 bilateral nerves) that were visually assessed by an expert (GX) in each subject (for a total of 168 TGNs evaluated in total in this experiment).

The three ROIs were drawn on the dMRI data using the *Editor* module in 3D Slicer (as illustrated in Fig. 1). In our study, we chose to draw ROIs directly on the dMRI data because multiple studies have shown dMRI-based ROIs are effective for TGN tracking and/or evaluation of TGN identification (Behan et al., 2017; Fujiwara et al., 2011; Kabasawa et al., 2007; Moon et al., 2018). In addition, the dMRI data under study had a high resolution ($1.25 \times 1.25 \times 1.25$ mm^3), which provided a good contrast for drawing ROIs. The ROI in MC was drawn on the mean $b = 0$ image from the coronal view. The computed trace map (see Section 2.1) was used to confirm the location of MC. The ROIs in CP and REZ were drawn on the mean DEC map of the DTI data from the coronal view. We chose the $b = 1000$ DEC map to draw these two ROIs because it gave a better visualization of REZ and CP than $b = 2000$ and $b = 3000$ DEC maps. The obtained ROIs were viewed on the $b = 2000$ and $b = 3000$ DEC maps and the corresponding T2w image to confirm accurate localization. The TGN was selected by finding the tractography streamlines that intersected the ROI(s) using the *Tractography ROI Selection* module in 3D Slicer. An exclusion of the streamlines crossing the hemispheres of the brain (an additional ROI was drawn at the midsagittal plane) was performed to be consistent with the dMRI-based TGN studies in the literature, where the ipsilateral TGN structure was primarily studied.

Expert rating was performed to choose the best selection results by visually assessing each tracked putative TGN, as follows: 1) a selection

Table 2
Anatomical rating scheme for expert anatomical evaluation of trigeminal nerve tractography

Anatomical criteria			Expert rating score
I. Identification of true positive structures	a. Branch-like structures present		Yes (1); No (0)
	b. Cisternal portion and T2 overlap	Overlap present	Yes (1); No (0)
		Good overlap	Yes (1); No (0)
	c. Mesencephalic trigeminal tract present		Yes (1); No (0)
	d. Spinal cord tract present		Yes (1); No (0)
II. Avoid false positive tracking	e. Avoid entering into temporal lobe		Yes (1); No (0)
	f. Avoid inferior cerebellar peduncle		Yes (1); No (0)
	g. Avoid middle cerebellar peduncle		Yes (1); No (0)

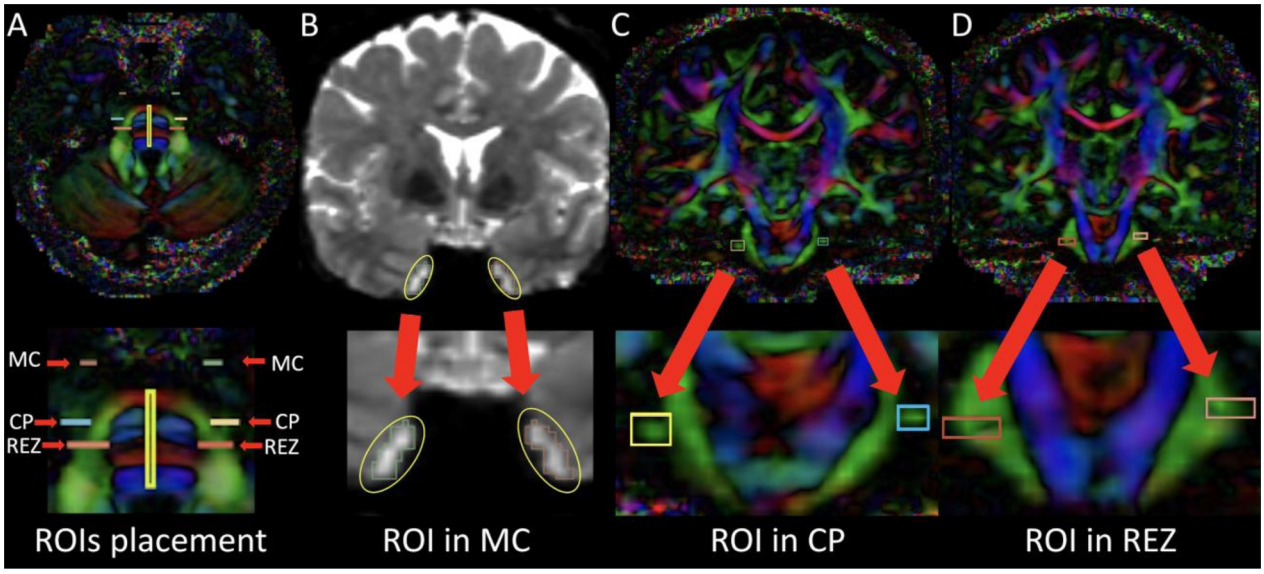

Fig. 1. ROIs for trigeminal nerve tracking. Six selection ROIs on bilateral sides and one exclusion ROI in the midline were drawn for every subject (A). The ROI in the Meckel's Cave (MC) was drawn on the mean b = 0 image from the coronal view (B), a second ROI was drawn at the cisternal portion (CP) of the TGN (C), and a third ROI was placed at REZ of the TGN (D) on the diffusion tensor map from the coronal view. (For interpretation of the references to colour in this figure legend, the reader is referred to the web version of this article.)

method should in general obtain visually reasonable TGNs across all of the six tracking strategies (based on our proposed anatomical criteria in Section 2.4), and 2) the selection method that used the lowest number of ROIs was preferable if two or more methods gave similar selection results (to minimize potential bias from including more ROIs).

2.3.2. Selection of the TGN in all tractography datasets

We then performed a ROI-based selection of the TGN in all tractography datasets, including 1T-1000, 1T-2000, 1T-3000, 2T-1000, 2T-2000, and 2T-3000. This used the best-performing ROI selection approach (*MC + CP* was employed as discussed in Section 3.2). This produced 12 TGNs per subject (6 tracking strategies x 2 bilateral nerves), for a total of 1104 TGNs across all subjects.

2.4. Anatomical assessment criteria and expert rating of the TGN

The resulting 1104 TGNs were then rated using expert judgment. Rating scores were given based on seven criteria we propose following the known anatomy of the TGN (Table 2). These criteria were developed in collaboration with a neuroanatomist (NM), and following the known anatomy of the TGN (Go et al., 2001; Joo et al., 2014). An expert rater (GX), who is a practicing neurosurgeon, visually assessed and rated each TGN by overlaying it on the structural T2-weighted image (on which the TGN was more visually apparent than on dMRI). The rating criteria enabled judgment of both true positives and false positives, and also included a comparison to the TGN anatomy as seen on T2-weighted images (Fig. 2). For this multimodal comparison, the streamline trajectory was compared to T2-weighted MRI in the cisternal portion of the TGN, and the overlap of the TGN on the two modalities was assessed. Anatomical criteria included the presence of any overlap (including over-estimation, under-estimation, or good overlap), followed by judgment of whether there was good overlap between the two modalities. Note that the three major branches of the trigeminal nerve could not be well traced anterior to Meckel's cave, and therefore we rated the presence of the initial branching (based on the presence of any branch-like structures).

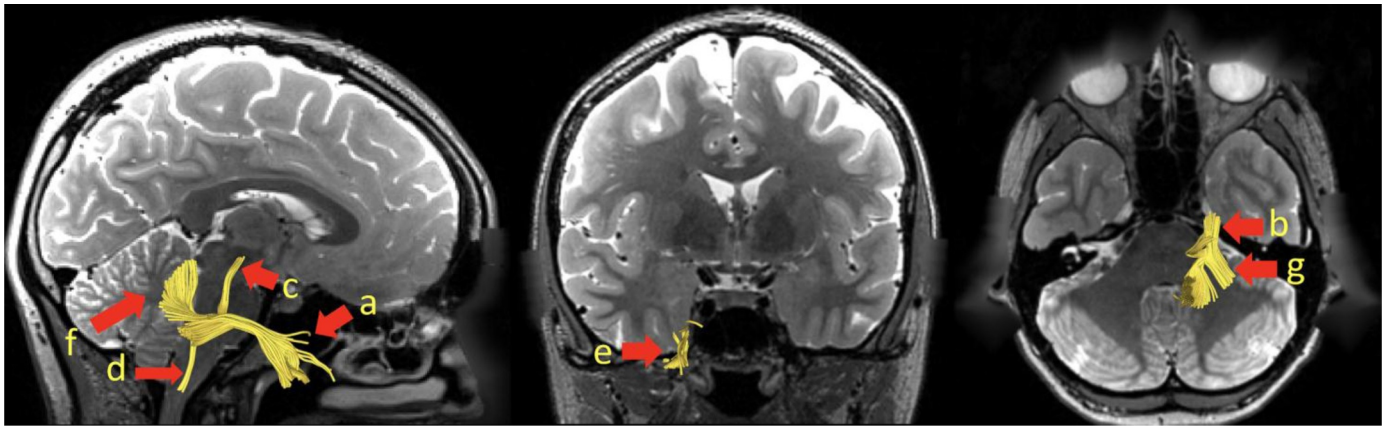

Fig. 2. Illustration of the anatomical assessment criteria of the TGN for expert evaluation. Sagittal, coronal, and axial views of an example TGN (yellow) are overlaid on T2-weighted MRI. Criteria include: (a) presence (or absence) of branch-like structure, (b) quality of cisternal portion and T2 overlap, (c) presence (or absence) of mesencephalic trigeminal tract, (d) presence (or absence) of spinal cord tract of the TGN, (e) avoiding entering (or entering) into temporal lobe, (f) avoiding (or entering) inferior cerebellar peduncle, and (g) avoiding (or entering) middle cerebellar peduncle.

2.5. Statistical analysis

Statistical analysis was performed to compare the TGN tracking strategies based on the expert rating scores. Because our rating scores are binary values, we chose the Cochran's Q test (Cochran, 1950) for statistical comparison among different TGN tracking strategies. (Cochran's Q test is a non-parametric statistical comparison method for differences between two or more groups of matched samples, where each sample has a binary outcome, e.g. 0 and 1.) First, to compare the performance of single-tensor and two-tensor tractography methods, we performed a two-group Cochran's *Q* test between the corresponding 1T-based and 2T-based results (i.e. 1T-1000 versus 2T-1000, 1T-2000 versus 2T-2000, and 1T-3000 versus 2T-3000, with false discovery rate (FDR) correction across the three comparisons). Then, to compare the performance of the different *b*-values, we compared across the three *b*-values under each tractography method (i.e., 1T-1000 versus 1T-2000 versus 1T-3000, and 2T-1000 versus 2T-2000 versus 2T-3000, with FDR correction across the three comparisons). A three-group Cochran's Q test comparing across the three strategies was performed, and if this was significant, it was followed by a two-group Cochran's Q test between each pair of strategies.

2.6. Expert intra- and inter-rater validation

To assess the reliability of the expert TGN assessment results, we included an inter-rater reliability validation and an intra-rater reliability validation. These experiments measured the joint probability of agreement, i.e., the percentage of ratings that are the same (Miller and Vanni, 2005). For the inter-rater validation, an additional expert rater (MAM), who is a practicing neurosurgeon, performed TGN rating based on the 7 proposed anatomical criteria. 12 HCP subjects were included in this experiment. For each of these subjects, the left TGNs obtained using the 6 tracking strategies were evaluated, for a total of 72 TGNs. We calculated the joint probability of agreement as the percentage of the 72

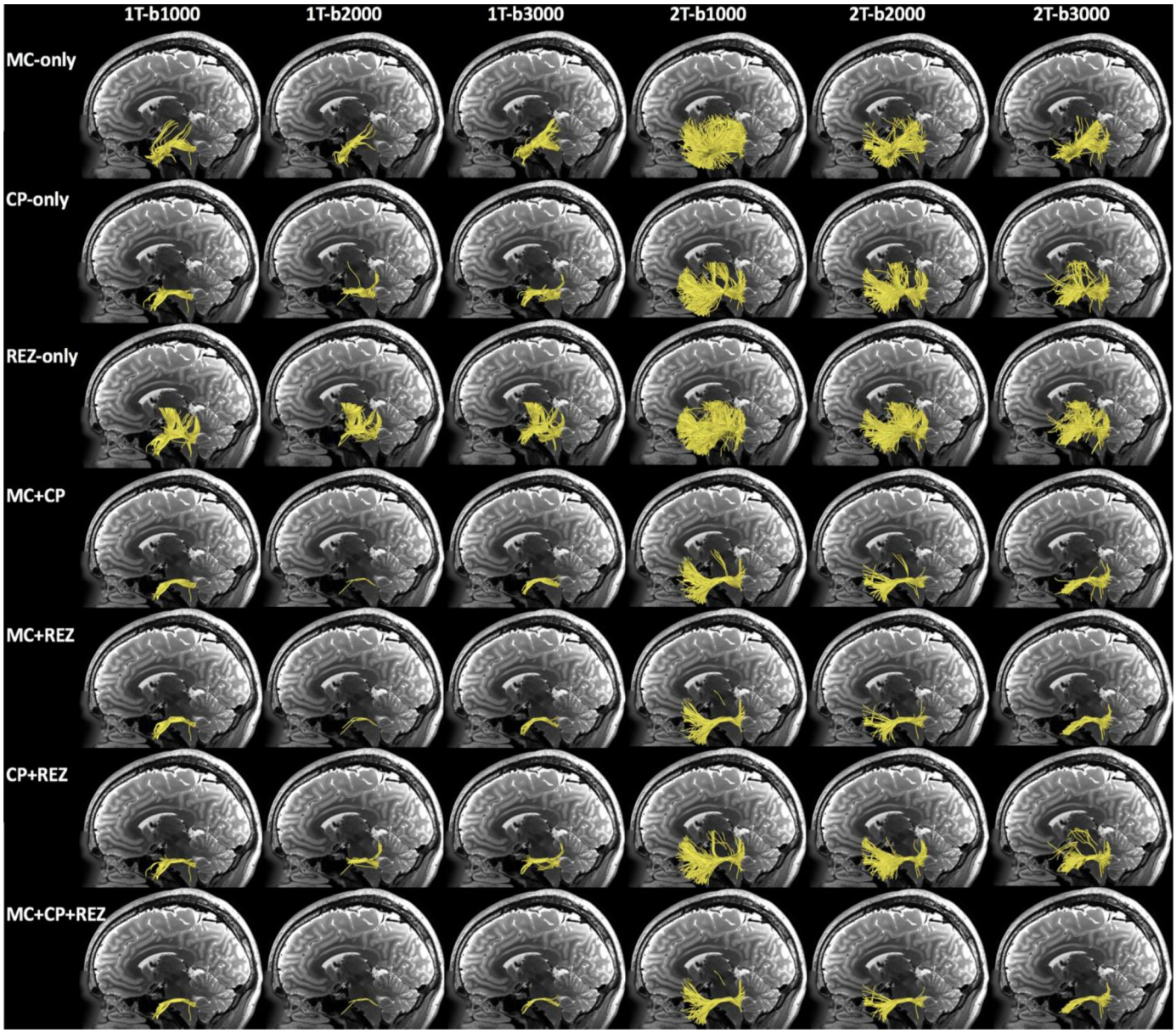

Fig. 3. Comparison of TGN selection results using different combinations of ROIs. Each column shows the putative TGNs obtained using the seven ROI selection methods, for a certain tracking strategy. The selected tractography streamlines (yellow) obtained from the data of one example HCP subject are displayed, overlaid on a T2-weighted sagittal image of the example subject. Abbreviations: MC – Meckel's Cave; CP – cisternal portion; REZ – root entry zone; TGN-trigeminal nerve. (For interpretation of the references to colour in this figure legend, the reader is referred to the web version of this article.)

TGNs given the same rating score by the two experts. For the intra-rater validation, the first expert rater (GX) repeated the TGN rating in the same 12 HCP subjects (72 TGNs) as used in the inter-rater validation. The joint probability of agreement with respect to the expert's previous rating was calculated as the percentage of the TGNs given the same rating score in both rating procedures.

3. Experimental results

3.1. Best-performing ROIs for selection of the TGN

For each of the ROI-selection methods, 100% of the putative TGNs were successfully identified in all testing subjects. In particular, in the three-ROI selection method (MC + CP + REZ) (where each selected TGN streamline traversed all three ROIs), all putative TGNs were detected, showing that each of the ROIs was effective for selection of TGN streamlines. Fig. 3 shows the comparison of TGN selection results using different combinations of ROIs from one example HCP subject. Using a single-ROI selection method (*MC-only, CP-only,* or *REZ-only*), the selected tractography streamlines contain many false positives with respect to the known anatomy of the TGN, in particular using the 2T-based tracking strategies. Using two-ROI selection methods (*MC + CP, MC + REZ,* or *CP + REZ)*, the obtained putative TGNs are more anatomically correct compared to those obtained using single-ROI selection methods. Using the three-ROI selection method (*MC + CP + REZ*), the obtained putative TGN is visually similar to those selected using two ROIs. Overall, the two-ROI selection methods in general produced better TGN selection results to balance between tracking an anatomically reasonable TGN and requiring the minimal number of ROIs. Based on visual assessment of 168 putative TGNs in this experiment, we chose the *MC + CP* selection method for use in this study. *MC + CP* gave better performance than the other two-ROI selection methods, where *MC + REZ* was overly restrictive (e.g., the mesencephalic trigeminal tract in 2T-1000 and 2T-2000 was excluded) and *CP + REZ* tended to give a noisier selection result (e.g., increased false positive streamlines in 2T-3000).

3.2. Expert rating scores based on the anatomical criteria

To illustrate the expert rating results, Fig. 4 gives a case illustration for a visual comparison of the TGNs obtained from the six tracking strategies in one example HCP subject.

Table 3 gives the overall results from the six compared TGN tracking strategies, in terms of the percentage of TGNs detected and the expert rating scores (expressed here as the percentage of TGNs satisfying each criterion). (See Supplementary Material 2 for raw data including the expert rating scores of each TGN from all subjects under study.) The percentage of TGNs detected was higher in the 2T-based methods than the 1T-based methods. See the following sections for statistical analyses of the expert rating scores. In addition, to evaluate the TGN tracking performance in different hemispheres, we also reported the percentage of TGNs detected and the expert rating scores in the left and right hemispheres separately (see Tables S2 and S3 in Supplementary Material 3). In general, the comparison results were consistent across the hemispheres, where the highest-performing strategies for each expert rating category were the same for the left and right hemispheres.

3.3. Comparison of 1T-based and 2T-based TGN tracking strategies

Table 4 gives the statistical comparison between 1T- and 2T-based TGN tracking strategies for each anatomical assessment criterion. Significantly higher expert rating scores were obtained using the 2T-based strategies in identifying true positive structures in all *b*-value acquisitions, except for the “Good overlap” criterion, in which the 1T methods

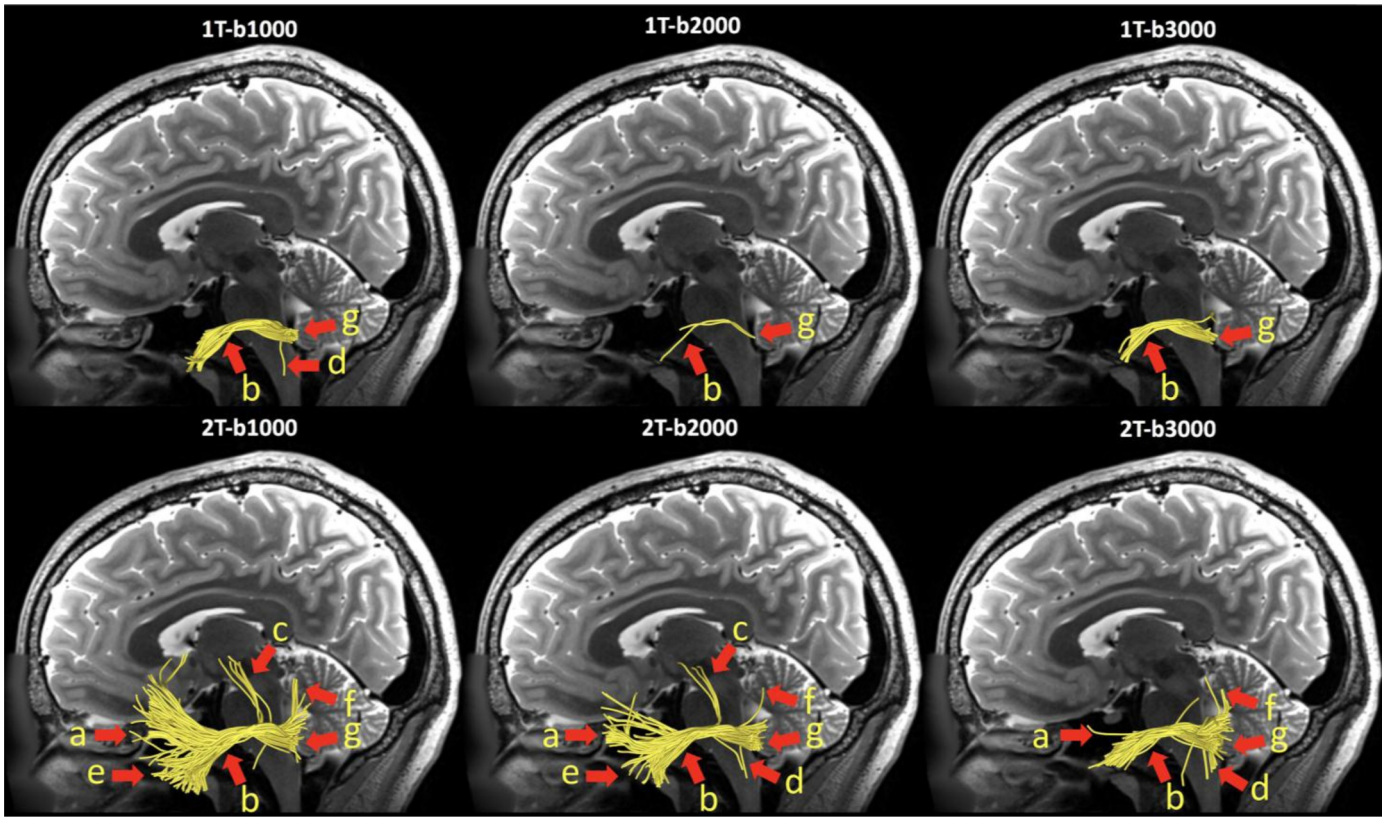

Fig. 4. Visual comparison of the TGNs derived from the six tracking strategies on the data from one example HCP subject. Criteria include: (a) branch-like structure, (b) cisternal portion, (c) mesencephalic trigeminal tract, (d) spinal cord tract of the TGN, (e) streamlines entering into temporal lobe, (f) streamlines entering inferior cerebellar peduncle, and (g) streamlines entering middle cerebellar peduncle.

Table 3
Overall results of six TGN tracking strategies, including the percentage of TGNs detected and the expert rating results for all TGNs. The rating results are given as the percentage of subjects in which each expert rating criterion was satisfied. In this way, higher percentages indicate better performance. The highest-performing strategies for each expert rating category are in bold. Where the top two highest-performing strategies are not significantly different (see following two tables for statistical comparison details), they are both shown in bold.

		1T-b1000	1T-b2000	1T-b3000	2T-b1000	2T-b2000	2T-b3000
Percentage of detected TGNs		97.83%	82.61%	90.22%	**100%**	**100%**	98.91%
True positive tracking							
a. Presence of branch-like structure		84.78%	51.63%	70.11%	**98.91%**	**98.37%**	94.57%
b. Presence of cisternal portion and T2 overlap	Overlap present	94.02%	74.46%	81.82%	**100.00%**	**100.00%**	97.28%
	Good overlap	**10.87%**	**11.96%**	4.89%	1.63%	2.72%	8.69%
c. Presence of mesencephalic trigeminal tract		25.00%	9.78%	8.15%	**37.50%**	26.09%	13.59%
d. Presence of spinal cord tract		11.41%	6.52%	9.24%	40.22%	**57.07%**	**56.52%**
Avoiding false positive tracking							
e. Avoid entering into temporal lobe		39.13%	**71.20%**	55.98%	1.09%	8.70%	33.70%
f. Avoid inferior cerebellar peduncle		57.61%	**72.83%**	54.89%	14.68%	15.77%	17.93%
g. Avoid middle cerebellar peduncle		0%	0%	0%	0%	0%	0%

performed significantly better for $b = 1000$ and 2000. (Note, however, that the "Good overlap" of TGN tractography was rarely obtained.) For all *b*-values, the 1T-based strategies obtained significantly higher performance on avoiding false positive tracking entering into the temporal lobe and ICP. All compared TGN tracking strategies suffered from false positive tracking of MCP, in all subjects under study.

3.4. Comparison results between TGN tracking strategies using different b-values

Table 5 summarizes the statistical analysis results across the 3 *b*-values. For almost all structures, TGN tracking performance was significantly different across the three *b*-values. Exceptions include the presence of the spinal cord tract using 1T tractography, the avoidance of the ICP using 2T tractography, and the avoidance of MCP with 1T and 2T tractography, which did not differ across *b*-values. Table 5 also includes pairwise comparisons between TGN tracking performance at different *b*-values.

3.5. Expert inter- and intra-rater validation

Table 6 gives the inter-rater and intra-rater validation results. In general, a high joint probability of agreement was obtained between the two expert raters, in particular on the criteria of T2 overlap present (97%) and avoiding middle cerebellar peduncle (100%). The joint probability of agreement on avoiding the inferior cerebellar peduncle was relatively low (60%), as the clinicians found that the inferior cerebellar peduncle was relatively difficult to locate on the T2w image. For the intra-rater validation, the repeated ratings from the same expert were highly reliable, where on average 90% of the rating scores were the same across the seven anatomical criteria.

4. Discussion

In the current study, we compared TGN tracking performance using dMRI data with different *b*-values, in combination with both single- and multi-tensor tractography methods. Our goal was to assess the advantages and limitations of these different strategies for identifying the anatomical regions of the TGN. To this end, we proposed seven anatomical criteria including true and false positive structures, and we performed an expert rating study of over 1,000 TGN visualizations. Overall, we have two main observations. First, we found that the two-tensor tractography method in general had better performance on identifying true positive structures including the branch-like structure, the cisternal portion, the mesencephalic trigeminal tract and the spinal cord tract of the TGN. On the other hand, the single-tensor tractography method was in general better at avoiding false positive tracking of streamlines that entered into the temporal lobe and the inferior cerebellar peduncle. However, all compared TGN tracking strategies suffered from false positive tracking of MCP in all subjects under study. (These findings were also confirmed based on a case illustration using dMRI data with a relatively low image resolution from a different acquisition site, as shown in Supplementary Material 4.) Second, TGN tracking performance was significantly different across the three *b*-values for almost all structures studied with either 1T or 2T tractography. Exceptions included the presence of the spinal cord tract using 1T tractography, the avoidance of the ICP using 2T tractography, and the avoidance of MCP with 1T and 2T tractography, which did not differ across *b*-values. The performance on these particular expert rating criteria was generally low (from 0% to 17.93% of subjects), so it is possible that an effect of b-value could be seen given future improvements to tracking methods.

In our initial ROI comparison experiment, we found that a two-ROI selection strategy using ROIs in the Meckel's Cave and in the cisternal

Table 4
Comparison between 1T- and 2T-based tracking strategies. The higher mean expert score is indicated using bold font. Asterisks indicate a significant difference based on the *p* value computed from a two-group Cochran's *Q* test (* represents $p < 0.05$; ** represents $p < 0.001$).

		$b = 1000$		b = 2000		b = 3000	
		1T	2T	1T	2T	1T	2T
True positive tracking							
a. Branch-like structure present		84.78%	**98.91%** **	51.63%	**98.47%** **	70.11%	**94.57%** **
b. Cisternal portion and T2 overlap	Overlap present	94.02%	**100.00%** **	74.46%	**100.00%** **	81.82%	**97.28%** **
	Good overlap	**10.87%** **	1.63%	**11.96%****	2.72%	4.89%	8.69%
c. Mesencephalic trigeminal tract		25.00%	**37.59%** *	9.78%	**26.09%** **	8.15%	**13.59%** *
d. Spinal cord tract present		11.41%	**40.22%** **	6.52%	**57.07%** **	9.24%	**56.52%** **
Avoid false positive tracking							
e. Avoid entering into temporal lobe		**39.13%** **	1.09%	**71.20%** **	8.70%	**55.98%** **	33.70%
f. Avoid inferior cerebellar peduncle		**57.61%** **	14.68%	**72.83%** **	15.77%	**54.89%** **	17.93%
g. Avoid middle cerebellar peduncle		0.00%	0.00%	0.00%	0.00%	0.00%	0.00%

Table 5
Statistical comparison of results across the three different *b*-value acquisitions, using 1T-based and 2T-based tracking strategies. Comparison is performed across the 3 *b*-values using a three-group Cochran's Q test, where $p < 0.05$ is considered to be significantly different. If this comparison is significant, it is followed by a pairwise comparison using a two-group Cochran's *Q* test, with FDR correction. Asterisks indicate a significant difference (* represents $p < 0.05$; ** represents $p < 0.001$; ">" or "<" in the parenthesis indicate if the performance is higher or lower in the first method).

		1T-based strategies				2T-based strategies			
		Three-strategy comparison (*p*-value)	Pairwise comparison			Three-strategy comparison (*p*-value)	Pairwise comparison		
			b1000 vs b2000	b1000 vs b3000	b2000 vs b3000		b1000 vs b2000	b1000 vs b3000	b2000 vs b3000
True positive tracking									
a. Branch-like structure present		$p < 0.001$ *	** (>)	** (>)	** (<)	$p = 0.012$ *		** (>)	** (>)
b. Cisternal portion and T2 overlap	Overlap present	$p < 0.001$ *	** (>)	** (>)	* (<)	$p = 0.006$ *		* (>)	* (>)
	Good overlap	$p = 0.035$ *		* (>)	* (>)	$p < 0.001$ *		* (<)	* (<)
c. Mesencephalic trigeminal tract		$p < 0.001$ *	** (>)	** (>)		$p < 0.001$ *	** (>)	** (>)	** (>)
d. Spinal cord tract present		$p = 0.055$				$p < 0.001$ *	** (<)	** (<)	
Avoid false positive tracking									
e. Avoid entering into temporal lobe		$p < 0.001$ *	** (<)	** (<)	** (>)	$p < 0.001$ *	** (<)	** (<)	** (<)
f. Avoid inferior cerebellar peduncle		$p < 0.001$ *	** (<)		** (>)	$p = 0.565$			
g. Avoid middle cerebellar peduncle		$p = 1.000$				$p = 1.000$			

Table 6
Expert inter- and intra-rater validation. The agreement is measured as the joint probability of agreement, i.e. the percentage of ratings that are the same.

		Inter-rater agreement	Intra-rater agreement
True positive tracking			
a. Presence of branch-like structure		81.94%	94.44%
b. Presence of cisternal portion and T2 overlap	Overlap present	97.22%	97.22%
	Good overlap	79.17%	88.89%
c. Presence of mesencephalic trigeminal tract		80.56%	79.17%
d. Presence of spinal cord tract		88.89%	94.72%
Avoiding false positive tracking			
e. Avoid entering into temporal lobe		79.17%	80.83%
f. Avoid inferior cerebellar peduncle		59.72%	79.17%
g. Avoid middle cerebellar peduncle		100%	100%

portion of the TGN gave the best TGN tracking result. In related work, a single-ROI TGN selection strategy was most commonly employed (see Table 1). However, our results on testing combinations of ROIs that are used in the literature indicated that using only one ROI generated many false positive streamlines for selection of the TGN, in particular using the 2-tensor tractography method. It is well known that multi-fiber models are more sensitive but can also generate more false positive fibers (Maier-Hein et al., 2017; Zhang et al., 2018). Thus, more ROIs are required due to the increased sensitivity.

We demonstrated that using a two-tensor fiber model had advantages for identifying true positive TGN structures compared to a single-tensor fiber model. In the literature of tractography-based TGN identification, while many studies applied a single-tensor fiber model (Chen et al., 2011; Coskun et al., 2017; Fujiwara et al., 2011; Hodaie et al., 2012; Kabasawa et al., 2007; Moon et al., 2018; Zolal et al., 2017), several other groups have investigated multi-fiber models and demonstrated the benefits of applying a higher-order fiber model. One research group applied two-tensor tractography methods for TGN tracking in multiple studies (Behan et al., 2017; Chen et al., 2016; Hung et al., 2017), and they demonstrated that a two-tensor fiber model allowed for identification of TGN structures that were unable to be seen using a one-tensor fiber model. For example, in (Behan et al., 2017), the authors showed that only streamlines entering into the cerebellar peduncle could be tracked using a DTI single-tensor tractography method, while using a two-tensor method, additional streamlines entering the brainstem could be tracked. In another study, Yoshino et al. applied multi-fiber DSI tractography, and they showed improvements of their method over standard DTI on reproducing multiple fiber crossings within the brainstem (Yoshino et al., 2016).

We compared TGN tracking results using dMRI data with three different *b*-values. In related work, most studies have used $b = 800$ (Kabasawa et al., 2007; Zolal et al., 2017) and $b = 1000$ (Behan et al., 2017; Chen et al., 2011, 2016; Coskun et al., 2017; Fujiwara et al., 2011; Hodaie et al., 2012; Hung et al., 2017). One group employed a DSI acquisition with 12 *b*-values (Yoshino et al., 2016). To our knowledge, this is the first work comparing TGN tracking results across different styles of dMRI acquisition.

We proposed seven anatomical criteria to assess the TGN tracking performance. These criteria included the presence of multiple expected anatomical segments of the TGN (true positive structures) and the presence of anatomically unexpected false positive tracking. To the best of our knowledge, these criteria provide the most comprehensive rating scheme in the literature. For the assessment of true positive structures, we included the cisternal portion of the TGN, which has been widely studied (Behan et al., 2017; Burkett et al., 2017; Fujiwara et al., 2011; Hodaie et al., 2012, 2010; Hung et al., 2017; Ishida et al., 2011; Jacquesson et al., 2018; Kabasawa et al., 2007; Lee et al., 2018; Ma et al., 2016; Moon et al., 2018)branch-like structures (Hodaie et al., 2010; Upadhyay et al., 2008; Yoshino et al., 2016) the spinal cord tract (Yoshino et al., 2016). Regarding false positive tracking, we proposed three criteria including the presence of fibers entering the temporal lobe, the inferior cerebellar peduncle, and the middle cerebellar peduncle. In the previous work, most studies focused on false positive streamlines entering the cerebellar peduncles (Behan et al., 2017; Chen et al., 2011, 2016; Hung et al., 2017; Jacquesson et al., 2018; Yoshino et al., 2016).

Next, we discuss detailed observations regarding the results for each anatomical assessment criterion. The cisternal portion of the TGN is the most widely studied (Behan et al., 2017; Burkett et al., 2017; Fujiwara et al., 2011; Hodaie et al., 2012, 2010; Hung et al., 2017; Ishida et al., 2011; Jacquesson et al., 2018; Kabasawa et al., 2007; Lee et al., 2018; Ma et al., 2016; Moon et al., 2018). One benefit of using this structure for TGN tracking performance evaluation is that its location can be seen on a T2-weighted image. In our study, we compared the overlap between the dMRI-based 3D trajectory of the TGN and its T2-based location and showed that all tracking strategies had relatively high performance (with overlap present in 80-100% of subjects), with the highest performance using two-tensor tracking with $b = 1000$ and $b = 2000$. However, the TGN obtained using dMRI tractography tended to be over- or underestimated in size, with very limited expert rating of "good overlap" (under 12% of subjects for all strategies).

Relatively fewer studies have investigated the branching of the TGN (Hodaie et al., 2010; Upadhyay et al., 2008; Yoshino et al., 2016). In our study, the highest performance was obtained using the two-tensor tractography method on the $b = 1000$ and $b = 2000$ acquisitions, where branching was observed in over 98% of subjects. However, with this increased performance there was a tradeoff regarding false positive tracking into the temporal lobe, which was present in over 90% of subjects.

One study has reported tracking the spinal cord tract of the TGN (Yoshino et al., 2016). We found that higher b-values ($b = 2000$ and 3000) using the two-tensor tractography had the best performance on tracking this structure. However, reliably tracking this structure is a challenge, as it was observed in under 60% of subjects.

In the present study, we proposed, for the first time, to investigate the mesencephalic trigeminal tract to evaluate TGN tracking performance. The mesencephalic trigeminal tract is an important portion of the TGN that conveys proprioceptive information from the teeth, masticatory muscles and temporomandibular joints (Shigenaga et al., 1989). In our study, we identified the putative mesencephalic trigeminal tract using dMRI tractography, and we showed that it could be best tracked using the two-tensor tractography method on the $b = 1000$ acquisition. However, it could only be tracked in 37.5% of subjects, so improvements in acquisition and/or tracking technology are needed to improve performance of tracking the mesencephalic trigeminal tract.

False positive tracking of the TGN has been reported in several studies, which have observed false positive streamlines entering the cerebellar peduncles (Behan et al., 2017; Chen et al., 2011, 2016; Hung et al., 2017; Jacquesson et al., 2018; Yoshino et al., 2016). In the present study, we separately rated false positive tracking into the inferior and middle cerebellar peduncles, as well as the temporal lobe. We found that one-tensor tractography on the $b = 2000$ acquisition had the best performance in avoiding the inferior cerebellar peduncle and the temporal lobe (where this false positive tracking was avoided in over 72% and 71% of subjects, respectively). However, this tracking strategy also had the lowest percentage of detected TGNs. False positive tracking into the middle cerebellar peduncle was a large challenge for all compared strategies, as this false positive tracking was present in 100% of subjects. This issue can be somewhat ameliorated by the addition of an exclusion ROI to remove these fibers, but unfortunately this strategy will remove a large number of fibers, reducing the possibility of identifying other structures.

Our intra- and inter-rater validation showed that the overall reliability of the proposed anatomical judgment criteria was high. The joint probability of agreement was on average 83% in the inter-rater rating validation, and it was on average 90% in the intra-rater validation. Specifically, inter- and intra-rater reliability was high on criteria including the presence of cisternal portion and T2 overlap, the presence of the spinal cord tract, and the presence of fibers entering the middle cerebellar peduncle, where the joint probabilities of agreement were all over 88%. High joint probabilities of agreement (around or over 80%) were obtained on the criteria of the presence of branch-like structures, the presence of good overlap of cisternal portion on T2, the presence of the mesencephalic trigeminal tract, and the presence of fibers entering the temporal lobe. The joint probability of agreement on avoiding the inferior cerebellar peduncle was relatively low (60% in the inter-rater validation), as the clinicians found that the inferior cerebellar peduncle was relatively difficult to locate on the T2w image.

Potential limitations of the present study, including suggested future work to address limitations, are as follows. First, to make our experimental evaluation simpler, we performed evaluation on the ipsilateral nerve only, as conducted in the previous studies (see Table 1). By “ipsilateral” in this context, we mean that we studied the nerve separately on each side of the head, while excluding any streamlines that crossed the midline. (All studies listed in Table 1 evaluated the ipsilateral TGN.) However, we note that the TGN is the largest cranial nerve and it includes an important portion that crosses to the contralateral side of the brainstem (Bathla and Hegde, 2013; Joo et al., 2014). Second, while we showed that branch-like structures could be successfully detected using the two-tensor tractography method on $b = 1000$ and $b = 2000$ data, the peripheral branches of the TGN (ophthalmic nerve, maxillary nerve and mandibular nerve) could not be clearly separated. The reasons for this include the complex skull base environment, which contains nerve, bone, air, soft tissue and cerebrospinal fluid. These anatomical structures could result in partial voluming of the voxels, which contain mixed information from multiple components, and susceptibility artifacts, in particular at the air/bone interfaces. Third, in this study, we applied the UKF tractography method for TGN tracking because of its high performance, as well as due to the fact that it allows for a fair comparison between one-tensor and two-tensor fiber models using the same underlying mathematical framework. Further work could include a comparison with prior single-tensor and two-tensor fiber tracking methods (e.g. the methods applied in (Chen et al., 2016)) and other advanced fiber tracking methods such as constrained spherical deconvolution (Jeurissen et al., 2011) and global tractography (Christiaens et al., 2015). Fourth, we performed an experiment to determine the best-performing tractography parameters in terms of the entire TGN. However, in the future it would be interesting to investigate if location-specific tractography parameters could improve performance in different TGN regions such as the cistern portion, the mesencephalic trigeminal tract, and the spinal cord tract. Fifth, while we checked the manually drawn ROIs on multiple images from the high-quality HCP to reduce effects from ROI selection, we acknowledge that potential operator bias may exist. Though we believe the impact of operator bias had minimal effect on the assessment of the different TGN tracking strategies, a further investigation could include a validation of inter-operator ROI selection. Six, in the present study, we used the high-quality HCP data to investigate TGN tracking performance. While the HCP protocol is known to provide an advanced dMRI acquisition, which is expected to better enable tracking of nerves than a clinical acquisition protocol, we still found untracked TGNs in 8% of the subjects under study. A further investigation could include other techniques, e.g. super-resolution reconstruction of dMRI data (Ning et al., 2016; Scherrer et al., 2012), for further TGN tracking improvements. Seventh, we focused on TGN tracking using dMRI data from healthy adults in the current study. Many research studies have suggested that TGNs are important for understanding and/or potential treatment of various neurological disorders (Barz et al., 1997; McGough et al., 2015; Schrader et al., 2011). As an initial attempt, we applied our method on dMRI data from a patient with Parkinson's disease (Parkinson's disease has been suggested to be closely related to the TGN (Tremblay et al., 2017)), as well as a healthy control involved in the same study (see Supplementary Material 4). For this particular case, we found the results from the Parkinson's disease patient were in general comparable to those from the healthy control. Further in-depth investigation is needed, in particular given the various types of neurological disorders. In particular, a future investigation could include validation in patients with TN lesions such as multiple sclerosis, trigeminal nerve tumor, trigeminal neuralgia, and others. Our method provides highly sensitive TGN tracking performance using multi-tensor tractography and enables identification of the smaller mesencephalic and spinal cord tracts of the TGN, which have been relatively less studied in previous work about neurological disorders. These structures can potentially be affected by diseases and the study of them can be helpful for further understanding of the pathologies. While this investigation is out of the scope of the present study, we believe this is an interesting future research work.

5. Conclusion

This is the first study to compare TGN tracking performance using dMRI data with different b-values, in combination with both single- and multi-tensor tractography methods. The two-tensor tractography method had better performance on identifying true positive structures,

while generating more false positive streamlines in comparison to the single-tensor tractography method. TGN tracking performance was significantly different across the three b-values for almost all structures studied. In general, $b = 1000$ and $b = 2000$ acquisitions provided the best-rated tracking results. Overall, the results of the study suggest that researchers and clinicians may benefit from tailoring their acquisition and tracking methodology to the specific anatomical portion of the TGN that is of the highest interest. In general, tracking of the cisternal portion and branching structure of the TGN was successful. However, tracking the smaller mesencephalic and spinal cord tracts of the TGN is quite challenging, while false positive connections to the temporal lobe and cerebellar peduncles are prevalent. Further research is needed to improve both sensitivity and specificity of the depiction of the TGN anatomy using dMRI.

CRediT authorship contribution statement

Guoqiang Xie: Conceptualization, Methodology, Data curation, Formal analysis, Writing - review & editing. **Fan Zhang:** Conceptualization, Methodology, Data curation, Formal analysis, Writing - review & editing, Software. **Laura Leung:** . **Michael A. Mooney:** Data curation, Formal analysis, Writing - review & editing. **Lorenz Epprecht:** Conceptualization, Data curation, Formal analysis, Writing - review & editing. **Isaiah Norton:** Software. **Yogesh Rathi:** Writing - review & editing, Software. **Ron Kikinis:** Data curation, Formal analysis, Writing - review & editing. **Ossama Al-Mefty:** Data curation, Formal analysis, Writing - review & editing. **Nikos Makris:** Data curation, Formal analysis, Writing - review & editing. **Alexandra J. Golby:** Conceptualization, Data curation, Formal analysis, Writing - review & editing. **Lauren J O'Donnell:** Conceptualization, Methodology, Data curation, Formal analysis, Writing - review & editing, Software.

Acknowledgments

We gratefully acknowledge funding provided by the following National Institutes of Health (NIH) grants: P41 EB015902, P41 EB015898, R01 MH074794, R01MH111917, R01 MH119222, R01 CA235589, HHSN261200800001E and U01 CA199459.

Supplementary materials

Supplementary material associated with this article can be found, in the online version, at doi:10.1016/j.nicl.2019.102160.

References

Balestrino, M., Leandri, M., 1997. Trigeminal neuralgia in pontine ischaemia. J. Neurol. Neurosurg. Psychiatry 62, 297–298.
Barz, S., Hummel, T., Pauli, E., Majer, M., Lang, C.J., Kobal, G., 1997. Chemosensory event-related potentials in response to trigeminal and olfactory stimulation in idiopathic Parkinson's disease. Neurology 49, 1424–1431.
Basser, P.J., Mattiello, J., LeBihan, D., 1994. MR diffusion tensor spectroscopy and imaging. Biophys. J. 66, 259–267.
Basser, P.J., Pajevic, S., Pierpaoli, C., Duda, J., Aldroubi, A., 2000. In vivo fiber tractography using DT-MRI data. Magn. Reson. Med. 44, 625–632.
Bathla, G., Hegde, A.N., 2013. The trigeminal nerve: an illustrated review of its imaging anatomy and pathology. Clin. Radiol. 68, 203–213.
Baumgartner, C., Michailovich, O., Levitt, J., Pasternak, O., Bouix, S., Westin, C., Rathi, Y., 2012. A unified tractography framework for comparing diffusion models on clinical scans. In: Computational Diffusion MRI Workshop of MICCAI, Nice, pp. 27–32.
Behan, B., Chen, D.Q., Sammartino, F., DeSouza, D.D., Wharton-Shukster, E., Hodaie, M., 2017. Comparison of diffusion-weighted MRI reconstruction methods for visualization of cranial nerves in posterior fossa surgery. Front. Neurosci. 11, 554.
Burkett, D.J., Garst, J.R., Hill, J.P., Kam, A., Anderson, D.E., 2017. Deterministic tractography of the descending tract of the spinal trigeminal nerve using diffusion tensor imaging. J. Neuroimaging 27, 539–544.
Casselman, J., Mermuys, K., Delanote, J., Ghekiere, J., Coenegrachts, K., 2008. MRI of the cranial nerves—more than meets the eye: technical considerations and advanced anatomy. Neuroimaging Clin. N. Am. 18, 197–231.
Chen, D.Q., DeSouza, D.D., Hayes, D.J., Davis, K.D., O'Connor, P., Hodaie, M., 2016. Diffusivity signatures characterize trigeminal neuralgia associated with multiple sclerosis. Mult. Scler. 22, 51–63.
Chen, D.Q., Quan, J., Guha, A., Tymianski, M., Mikulis, D., Hodaie, M., 2011. Three-dimensional in vivo modeling of vestibular schwannomas and surrounding cranial nerves with diffusion imaging tractography. Neurosurgery 68, 1077–1083.
Chen, Z., Tie, Y., Olubiyi, O., Zhang, F., Mehrtash, A., Rigolo, L., Kahali, P., Norton, I., Pasternak, O., Rathi, Y., Golby, A.J., O'Donnell, L.J., 2016. Corticospinal tract modeling for neurosurgical planning by tracking through regions of peritumoral edema and crossing fibers using two-tensor unscented Kalman filter tractography. Int. J. Comput. Assist. Radiol. Surg. 11, 1475–1486.
Christiaens, D., Reisert, M., Dhollander, T., Sunaert, S., Suetens, P., Maes, F., 2015. Global tractography of multi-shell diffusion-weighted imaging data using a multi-tissue model. Neuroimage 123, 89–101.
Ciftci, E., Anik, Y., Arslan, A., Akansel, G., Sarisoy, T., Demirci, A., 2004. Driven equilibrium (drive) MR imaging of the cranial nerves V–VIII: comparison with the T2-weighted 3D TSE sequence. Eur. J. Radiol. 51, 234–240.
Cochran, W.G., 1950. The comparison of percentages in matched samples. Biometrika 37, 256–266.
Coskun, O., Ucar, M., Vuralli, D., Yildirim, F., Cetinkaya, R., Akin Takmaz, S., Ucler, S., 2017. MR tractography in short lasting unilateral neuralgiform headache attacks with conjunctival injection and tearing (SUNCT) patients: case reports. Pain Med. 18, 1377–1381.
Cruccu, G., Finnerup, N.B., Jensen, T.S., Scholz, J., Sindou, M., Svensson, P., Treede, R.-D., Zakrzewska, J.M., Nurmikko, T., 2016. Trigeminal neuralgia: New classification and diagnostic grading for practice and research. Neurology 87, 220–228.
Descoteaux, M., Angelino, E., Fitzgibbons, S., Deriche, R., 2007. Regularized, fast, and robust analytical Q-ball imaging. Magn. Reson. Med. 58, 497–510.
Fujiwara, S., Sasaki, M., Wada, T., Kudo, K., Hirooka, R., Ishigaki, D., Nishikawa, Y., Ono, A., Yamaguchi, M., Ogasawara, K., 2011. High-resolution diffusion tensor imaging for the detection of diffusion abnormalities in the trigeminal nerves of patients with trigeminal neuralgia caused by neurovascular compression. J. Neuroimaging 21, e102–e108.
Glasser, M.F., Sotiropoulos, S.N., Wilson, J.A., Coalson, T.S., Fischl, B., Andersson, J.L., Xu, J., Jbabdi, S., Webster, M., Polimeni, J.R., Van Essen, D.C., Jenkinson, M., Consortium, WU-Minn HCP, 2013. The minimal preprocessing pipelines for the Human Connectome Project. Neuroimage 80, 105–124.
Go, J.L., Kim, P.E., Zee, C.S., 2001. The trigeminal nerve. Semin. Ultrasound CT MR 22, 502–520.
Golby, A.J., Norbash, A., Silverberg, G.D., 1998. Trigeminal neuralgia resulting from infarction of the root entry zone of the trigeminal nerve: case report. Neurosurgery 43, 620–623.
Gong, S., Zhang, F., Norton, I., Essayed, W.I., Unadkat, P., Rigolo, L., Pasternak, O., Rathi, Y., Hou, L., Golby, A.J., O'Donnell, L.J., 2018. Free water modeling of peritumoral edema using multi-fiber tractography: application to tracking the arcuate fasciculus for neurosurgical planning. PLoS One 13, e0197056.
Haviv, Y., Zadik, Y., Sharav, Y., Benoliel, R., 2014. Painful traumatic trigeminal neuropathy: an open study on the pharmacotherapeutic response to stepped treatment. J. Oral Facial Pain Headache 28, 52–60.
Hodaie, M., Chen, D.Q., Quan, J., Laperriere, N., 2012. Tractography delineates microstructural changes in the trigeminal nerve after focal radiosurgery for trigeminal neuralgia. PLoS One 7, e32745.
Hodaie, M., Quan, J., Chen, D.Q., 2010. In vivo visualization of cranial nerve pathways in humans using diffusion-based tractography. Neurosurgery 66, 788–795 discussion 795–6.
Hung, P.S.-P., Chen, D.Q., Davis, K.D., Zhong, J., Hodaie, M., 2017. Predicting pain relief: use of pre-surgical trigeminal nerve diffusion metrics in trigeminal neuralgia. Neuroimage Clin. 15, 710–718.
Ishida, G., Oishi, M., Fukuda, M., Sato, M., Fujii, Y., 2011. Depiction of the trigeminal nerve deviated by a tumor lesion, using probabilistic diffusion tensor tractography. Neurol. Surg. 39, 255–262.
Jacquesson, T., Frindel, C., Kocevar, G., Berhouma, M., Jouanneau, E., Attyé, A., Cotton, F., 2018. Overcoming challenges of cranial nerve tractography: a targeted review. Neurosurgery.
Jeurissen, B., Leemans, A., Jones, D.K., Tournier, J.-D., Sijbers, J., 2011. Probabilistic fiber tracking using the residual bootstrap with constrained spherical deconvolution. Hum. Brain Mapp. 32, 461–479.
Joo, W., Yoshioka, F., Funaki, T., Mizokami, K., Rhoton Jr, A.L., 2014. Microsurgical anatomy of the trigeminal nerve. Clin. Anat. 27, 61–88.
Kabasawa, H., Masutani, Y., Aoki, S., Abe, O., Masumoto, T., Hayashi, N., Ohtomo, K., 2007. 3T PROPELLER diffusion tensor fiber tractography: a feasibility study for cranial nerve fiber tracking. Radiat. Med. 25, 462–466.
Lee, C.-C., Chong, S.T., Chen, C.-J., Hung, S.-C., Yang, H.-C., Lin, C.-J., Wu, C.-C., Chung, W.-Y., Guo, W.-Y., Pan, D.H.-C., Wu, H.-M., Sheehan, J.P., Lin, C.-P., 2018. The timing of stereotactic radiosurgery for medically refractory trigeminal neuralgia: the evidence from diffusion tractography images. Acta Neurochir. 160, 977–986.
Li, T., Sheng, L., Chunyan, C., Haoqiang, H., Kangqiang, P., Xiao, G., Lizhi, L., 2017. The significance of diffusion tensor magnetic resonance imaging for patients with nasopharyngeal carcinoma and trigeminal nerve invasion. Medicine 96, e6072.
Liao, R., Ning, L., Chen, Z., Rigolo, L., Gong, S., Pasternak, O., Golby, A.J., Rathi, Y., O'Donnell, L.J., 2017. Performance of unscented Kalman filter tractography in edema: analysis of the two-tensor model. Neuroimage Clin. 15, 819–831.
Liu, Y., Li, J., Butzkueven, H., Duan, Y., Zhang, M., Shu, N., Li, Y., Zhang, Y., Li, K., 2013. Microstructural abnormalities in the trigeminal nerves of patients with trigeminal neuralgia revealed by multiple diffusion metrics. Eur. J. Radiol. 82, 783–786.
Love, S., Coakham, H.B., 2001. Trigeminal neuralgia: pathology and pathogenesis. Brain

124, 2347–2360.
Ma, J., Su, S., Yue, S., Zhao, Y., Li, Y., Chen, X., Ma, H., 2016. Preoperative visualization of cranial nerves in skull base tumor surgery using diffusion tensor imaging technology. Turk. Neurosurg. 26, 805–812.
Maarbjerg, S., Di Stefano, G., Bendtsen, L., Cruccu, G., 2017. Trigeminal neuralgia – diagnosis and treatment. Cephalalgia 37, 648–657.
Maier-Hein, K.H., Neher, P.F., Houde, J.-C., Côté, M.-A., Garyfallidis, E., Zhong, J., Chamberland, M., Yeh, F.-C., Lin, Y.-C., Ji, Q., Reddick, W.E., Glass, J.O., Chen, D.Q., Feng, Y., Gao, C., Wu, Y., Ma, J., Renjie, H., Li, Q., Westin, C.-F., Deslauriers-Gauthier, S., González, J.O.O., Paquette, M., St-Jean, S., Girard, G., Rheault, F., Sidhu, J., Tax, C.M.W., Guo, F., Mesri, H.Y., Dávid, S., Froeling, M., Heemskerk, A.M., Leemans, A., Boré, A., Pinsard, B., Bedetti, C., Desrosiers, M., Brambati, S., Doyon, J., Sarica, A., Vasta, R., Cerasa, A., Quattrone, A., Yeatman, J., Khan, A.R., Hodges, W., Alexander, S., Romascano, D., Barakovic, M., Auría, A., Esteban, O., Lemkaddem, A., Thiran, J.-P., Cetingul, H.E., Odry, B.L., Mailhe, B., Nadar, M.S., Pizzagalli, F., Prasad, G., Villalon-Reina, J.E., Galvis, J., Thompson, P.M., Requejo, F.D.S., Laguna, P.L., Lacerda, L.M., Barrett, R., Dell'Acqua, F., Catani, M., Petit, L., Caruyer, E., Daducci, A., Dyrby, T.B., Holland-Letz, T., Hilgetag, C.C., Stieltjes, B., Descoteaux, M., 2017. The challenge of mapping the human connectome based on diffusion tractography. Nat. Commun. 8, 1349.
Malcolm, J.G., Shenton, M.E., Rathi, Y., 2010. Filtered multitensor tractography. IEEE Trans. Med. Imaging 29, 1664–1675.
McGough, J.J., Loo, S.K., Sturm, A., Cowen, J., Leuchter, A.F., Cook, I.A., 2015. An eight-week, open-trial, pilot feasibility study of trigeminal nerve stimulation in youth with attention-deficit/hyperactivity disorder. Brain Stimul. 8, 299–304.
Miller, K.J., Vanni, M., 2005. Inter-rater agreement measures and the refinement of metrics in the PLATO MT evaluation paradigm. ADA456393, 9.
Moon, H.C., You, S.-T., Baek, H.M., Jeon, Y.J., Park, C.-A., Cheong, J.J., Lee, Y.J., Park, Y.S., 2018. 7.0 Tesla MRI tractography in patients with trigeminal neuralgia. Magn. Reson. Imaging 54, 265–270.
Neetu, S., Sunil, K., Ashish, A., Jayantee, K., Usha Kant, M, 2016. Microstructural abnormalities of the trigeminal nerve by diffusion-tensor imaging in trigeminal neuralgia without neurovascular compression. Neuroradiol. J. 29, 13–18.
Ning, L., Laun, F., Gur, Y., DiBella, E.V.R., Deslauriers-Gauthier, S., Megherbi, T., Ghosh, A., Zucchelli, M., Menegaz, G., Fick, R., St-Jean, S., Paquette, M., Aranda, R., Descoteaux, M., Deriche, R., O'Donnell, L., Rathi, Y., 2015. Sparse Reconstruction Challenge for diffusion MRI: validation on a physical phantom to determine which acquisition scheme and analysis method to use? Med. Image Anal. 26, 316–331.
Ning, L., Setsompop, K., Michailovich, O., Makris, N., Shenton, M.E., Westin, C.-F., Rathi, Y., 2016. A joint compressed-sensing and super-resolution approach for very high-resolution diffusion imaging. Neuroimage 125, 386–400.
Norton, I., Essayed, W.I., Zhang, F., Pujol, S., Yarmarkovich, A., Golby, A.J., Kindlmann, G., Wassermann, D., Estepar, R.S.J., Rathi, Y., Pieper, S., Kikinis, R., Johnson, H.J., Westin, C.-F., O'Donnell, L.J., 2017. SlicerDMRI: open source diffusion mri software for brain cancer research. Cancer Res. 77, e101–e103.
O'Donnell, L.J., Suter, Y., Rigolo, L., Kahali, P., Zhang, F., Norton, I., Albi, A., Olubiyi, O., Meola, A., Essayed, W.I., Unadkat, P., Ciris, P.A., Wells 3rd, W.M., Rathi, Y., Westin, C.-F., Golby, A.J., 2017. Automated white matter fiber tract identification in patients with brain tumors. Neuroimage Clin. 13, 138–153.
Qazi, A.A., Radmanesh, A., O'Donnell, L., Kindlmann, G., Peled, S., Whalen, S., Westin, C.-F., Golby, A.J., 2009. Resolving crossings in the corticospinal tract by two-tensor streamline tractography: Method and clinical assessment using fMRI. Neuroimage 47 (Suppl 2), T98–106.
Reddy, C.P., Rathi, Y., 2016. Joint multi-fiber NODDI parameter estimation and tractography using the unscented information filter. Front. Neurosci. 10, 166.
Rousseau, A., Nasser, G., Chiquet, C., Barreau, E., Gendron, G., Kaswin, G., M'Garrech, M., Benoudiba, F., Ducreux, D., Labetoulle, M., 2015. Diffusion tensor magnetic resonance imaging of trigeminal nerves in relapsing herpetic keratouveitis. PLoS One 10, e0122186.
Scherrer, B., Gholipour, A., Warfield, S.K., 2012. Super-resolution reconstruction to increase the spatial resolution of diffusion weighted images from orthogonal anisotropic acquisitions. Med. Image Anal. 16, 1465–1476.
Schrader, L.M., Cook, I.A., Miller, P.R., Maremont, E.R., DeGiorgio, C.M., 2011. Trigeminal nerve stimulation in major depressive disorder: first proof of concept in an open pilot trial. Epilepsy Behav. 22 (3), 475–478.
Shapey, J., Vos, S., Vercauteren, T., Bradford, R., Saeed, S., Bisdas, S., Ourselin, S., 2019. Clinical applications for diffusion MRI and tractography of cranial nerves within the posterior fossa: a systematic review. Front. Neurosci. 13, 23.
Shigenaga, Y., Doe, K., Suemune, S., Mitsuhiro, Y., Tsuru, K., Otani, K., Shirana, Y., Hosoi, M., Yoshida, A., Kagawa, K., 1989. Physiological and morphological characteristics of periodontal mesencephalic trigeminal neurons in the cat–intra-axonal staining with HRP. Brain Res. 505, 91–110.
Suzuki, M., Yoshino, N., Shimada, M., Tetsumura, A., Matsumura, T., Fukayama, H., Kurabayashi, T., 2015. Trigeminal neuralgia: differences in magnetic resonance imaging characteristics of neurovascular compression between symptomatic and asymptomatic nerves. Oral Surg. Oral Med. Oral Pathol. Oral Radiol. 119, 113–118.
Tremblay, C., Durand Martel, P., Frasnelli, J., 2017. Trigeminal system in Parkinson's disease: a potential avenue to detect Parkinson-specific olfactory dysfunction. Parkinsonism Relat. Disord. 44, 85–90.
Tsutsumi, S., Ono, H., Yasumoto, Y., Ishii, H., 2018. The trigeminal root: an anatomical study using magnetic resonance imaging. Surg. Radiol. Anat. 40 (12), 1397–1403.
Upadhyay, J., Knudsen, J., Anderson, J., Becerra, L., Borsook, D., 2008. Noninvasive mapping of human trigeminal brainstem pathways. Magn. Reson. Med. 60, 1037–1046.
Van Essen, D.C., Smith, S.M., Barch, D.M., Behrens, T.E.J., Yacoub, E., Ugurbil, K., Consortium, WU-Minn HCP, 2013. The WU-Minn Human Connectome Project: an overview. Neuroimage 80, 62–79.
Wei, P.-H., Qi, Z.-G., Chen, G., Li, M.-C., Liang, J.-T., Guo, H.-C., Bao, Y.-H., Hao, Q., 2016. Identification of cranial nerves around trigeminal schwannomas using diffusion tensor tractography: a technical note and report of 3 cases. Acta Neurochir. 158, 429–435.
Woolfall, P., Coulthard, A., 2001. Pictorial review: Trigeminal nerve: anatomy and pathology. Br. J. Radiol. 74, 458–467.
Yadav, Y.R., Nishtha, Y., Sonjjay, P., Vijay, P., Shailendra, R., Yatin, K., 2017. Trigeminal neuralgia. Asian J. Neurosurg. 12, 585–597.
Yoshino, M., Abhinav, K., Yeh, F.-C., Panesar, S., Fernandes, D., Pathak, S., Gardner, P.A., Fernandez-Miranda, J.C., 2016. Visualization of cranial nerves using high-definition fiber tractography. Neurosurgery 79, 146–165.
Yoshino, N., Akimoto, H., Yamada, I., Nagaoka, T., Tetsumura, A., Kurabayashi, T., Honda, E., Nakamura, S., Sasaki, T., 2003. Trigeminal neuralgia: evaluation of neuralgic manifestation and site of neurovascular compression with 3D CISS MR imaging and MR angiography. Radiology 228, 539–545.
Zhang, F., Wu, Y., Norton, I., Rigolo, L., Rathi, Y., Makris, N., O'Donnell, L.J., 2018. An anatomically curated fiber clustering white matter atlas for consistent white matter tract parcellation across the lifespan. Neuroimage 179, 429–447.
Zolal, A., Sobottka, S.B., Podlesek, D., Linn, J., Rieger, B., Juratli, T.A., Schackert, G., Kitzler, H.H., 2017. Comparison of probabilistic and deterministic fiber tracking of cranial nerves. J. Neurosurg. 127, 613–621.